PAPER

Check for updates

Ni–Fe bimetallic catalysts with high dispersion supported by SBA-15 evaluated for the selective oxidation of benzyl alcohol to benzaldehyde

V. L. Mangesh,[a] Murali Govindarajan,[a] Rama Bhadri Raju Chekuri,[b] Tamizhdurai Perumal, [iD] *[c] Kumaran Rajendran,[c] Kavitha Chandrasekaran,[c] Nadavala Siva Kumar, [iD] [d] Praveen Kumar Basivi, [iD] [e] Salwa B. Alreshaidan[f] and Ahmed S. Al-Fatesh[d]

A wetness impregnation method was used to impregnate the substrate with a substantial quantity of oleic acid together with a metal precursor, leading to significantly dispersed Ni–Fe bimetallic catalysts based on mesoporous SBA-15. Using a wide variety of characterization methods, such as XRD, BET, and TEM Analysis, the physiochemical properties of the catalyst were determined. The addition of the metal does not have any effect on the structural characteristics of the SBA-15 catalyst, as validated by transmission electron microscopy (TEM), which shows that the prepared SBA-15 supported catalyst has a hexagonal mesoporous structure. The catalytic capabilities of the Ni–Fe-SBA-15 catalysts were evaluated in the conversion of BzOH using *tert*-butyl hydroperoxide (TBHP) as an oxidant and acetonitrile as a solvent. The Ni/Fe-SBA-15 (NFS-15) catalytic composition is the best of the developed catalysts, with a maximum conversion of 98% and a selectivity of 99%. In-depth investigations were conducted into the molar ratio of TBHP to BzOH, the dosage of the catalyst, the reaction rate, temperature, and solvent. The recycling investigations indicate that the synthesized Ni/Fe-SBA-15 (NFS-15) catalyst seems to be more durable up to seven successive cycles.

1. Introduction

Industries use selective oxidation techniques to convert alcohols into aldehydes and ketones.[1–4] Finding high-purity aldehydes at a reasonable cost is still a top objective for researchers.[5,6] Traditionally, we generated the hazardous organic waste, such as benzaldehyde, *via* toluene, benzyl chloride, and hydrolysis, respectively.[7] This conversion is more expensive overall[9–12] despite its limited selectivity, loss of conversion, toxic by-products, and substrate specificity.[8] Researchers employed liquid-phase selective oxidation with a noble metal catalyst and a variety of oxidants to get around these constraints.[13–16] Hydrogen peroxide (H_2O_2) is a powerful oxidizing agent that is also good for the environment and contains more active oxygen.[17–20] The inability to reuse the catalyst and the challenge of separating it from the catalytic system are two drawbacks of homogeneous catalysis.[21]

As a result, researchers are becoming more interested in the synthesis of affordable and environmentally acceptable solid acid catalysts.[22] The activity of the catalysts can be further increased by supporting materials.[23] Mahmoud Nasrollahzadeh and other researchers thoroughly evaluated the preferential oxidation of alcohols enabled by polymers.[24] Because of its significant surface area and well-defined high porosity, ordered mesoporous silica is thought to have better catalyst support.[25] In many heterogeneous catalyzes, metal catalysts, including Ru,[26] Co,[27] Au,[28] and Pd,[29] are used. Additionally, benzyl alcohol was catalytically converted using an SBA-15-assisted Au–Pd catalyst.[30] The expense of oxidation procedures is raised by the noble metal's high price and agglomeration on the support surface.[31] However, oxidation catalysts made of nickel are thought to be superior to those made of iron. This is attributed to stable oxide (nickel oxide) formation, which results in the catalytic abilities of semiconductor metal oxide rather than metal catalytic properties.[32]

Because of its good chemical stability and possible catalytic uses, Ni/Fe is a great option.[33] It has been extensively used in the photocatalytic reduction of CO_2, photocatalytic splitting of

[a]Department of Mechanical Engineering, Koneru Lakshmaiah Education Foundation, Vaddeswaram, Guntur, Andhra Pradesh 522502, India

[b]Sagi Rama Krishnam Raju Engineering College, Bhimavaram-534204, Andhra Pradesh, India

[c]Department of Chemistry, Dwaraka Doss Goverdhan Doss Vaishnav College (Autonomous) (Affiliated to the University of Madras, Chennai), 833, Gokul Bagh, EVR Periyar Road, Arumbakkam, Chennai 600 106, Tamil Nadu, India. E-mail: tamizhvkt2010@gmail.com; Tel: +91-9677146579

[d]Department of Chemical Engineering, King Saud University, P.O. Box 800, Riyadh 11421, Saudi Arabia. E-mail: snadavala@ksu.edu.sa; Tel: +966-537228108

[e]Pukyong National University Industry-University Cooperation Foundation, Pukyong National University, Busan 48513, Republic of Korea

[f]Department of Chemistry, Faculty of Science, King Saud University, P.O. Box 800, Riyadh 11451, Saudi Arabia

water, and photocatalytic synthesis of hydrogen.[34] Due to its exceptional photocatalytic activity, this comes from a quick and effective charge change between the oxidation states and has attracted a lot of attention.[35,36] The electrical configuration of the metal may be rapidly and drastically changed to perfectly accommodate its immediate surroundings.[37] Recently, Ni/Fe has been employed in the selective oxidation of benzyl alcohol as a substrate for Au–Pd nanoparticles and as a catalyst or photocatalyst. A photocatalyst made of Ni/Fe was also employed with SBA-15 as a support.[38,39] Researchers were synthesised the series of mesoporous Ni_xCo_y/SBA-15 catalysts with different Ni/Co ratios for the selective oxidation of alcohol using oxygen as the sole oxidant and it displayed the best catalytic performance with a benzyl alcohol conversion of 96.2%.[40] However, selective oxidation is used for the majority of the aforementioned processes. CeO_2, MnO_2, and Ni–Fe composites oxidation catalytic agents were created by Xiaodong Zhang *et al.* and investigated in the process of oxidizing CO and toluene.[41]

Oleic acid inhibits nanoparticles against agglomeration by providing steric stability against van der Waals along with magnetic attractive interactions.[42] Gong *et al.* investigated the influence of only one dosage of oleic acid (4 g in 100 ml) on the structural features of Fe_3O_4 nanoparticles. They observed that oleic acid, particularly present in the form of a bilayer, inhibit Ostwald ripening and promotes the formation of monodispersed magnetic nanospheres.[43] In the instance of Co nanoparticles, an oleic acid/cobalt ratio of 0.15 resulted in erratically formed black precipitates. Conversely, as the oleic acid molar ratio reached to 0.6, the capping agent developed an extremely dense monolayer on the outermost layer of the nanoparticles, which restored them against agglomeration and also prohibited the Co from oxidizing in the air.[44] However, as reported earlier, owing to the efficiency of oleic acid involved in the synthesis of the catalysts, likely as a result of the synthesis of metal oleate species, which stops the particles from clumping together during calcination. Additionally, the calcination process causes the metallic oxides to self-assemble, which results in significant dispersion and core–shell metal particles.

Investigations on the selective oxidation of benzyl alcohol utilizing Ni/Fe and SBA-15 in the liquid phase are still needed. The particle size, the kind of support, and the interaction between the support and the Ni/Fe catalyst are some of the factors that affect the Ni/Fe catalyst's ability to catalyze. This study involved the development of Ni/Fe-SBA-15 catalysts for the selective oxidation of benzyl alcohol (BzOH). In-depth research was done on the factors, such as catalyst quantity, metal loading, the substrate to oxidant ratio, and reaction temperature, that affect the efficiency of the oxidation from a catalytic perspective. The regeneration powers of the catalyst were also investigated in this work.

2. Experimental information

2.1. Preparation of catalysts and supports

Previous studies have shown that acidic conditions can be exploited to produce Ni–Fe bimetallic supported SBA-15 catalysts.[45] The Ni–Fe loaded SBA-15 was prepared in the manner described below. Add 4 grams of P123, a triblock co-polymer (Mol. Wt 5800) to 20 ml of HCl and 130 ml of water. TEOS (14 ml) is added, and the mixture was subjected to thorough stirring. Nickel nitrate and iron nitrate were added to the mixture, and stirred for 7.5 h at 45 °C. Afterward, the mixture was allowed to age for 15.5 hours at 80 °C and cooled down. The cooled precipitate was dried, filtered, and washed in 25 ml water. Post-synthesis, the product was calcined for 6 hours at a temperature of 550 °C with a heating rate of 1 °C min^{-1} and progressively cooled.[46]

Two sets of Ni–Fe bimetallic catalysts, each with a 7% metal loading (5 wt% Ni-2 wt% Fe/SBA-15 and 4 wt% Ni-3 wt% Fe/SBA-15), have been made, and compared with a mono metal catalyst comprising 7% Ni/SBA-15. Iron(III) nitrate nonahydrate and nickel(VI) nitrate hexahydrate, respectively, served as the precursors for the nickel and iron. Our previously reported core–shell precursor with *in situ* self-assembly technique was used to make the catalysts. Using an incipient wetness impregnation technique, a small amount of oleic acid (OA), nOA/n metal is, controlled at a molar ratio of 0.30, was utilised in this approach. The dissolved iron(III) nitrate nonahydrate and nickel hydrate hexahydrate were added, thoroughly mixed, and then combined with the SBA-15 support. The samples were aged for 12 h and then dried for around 6 h at 60 °C while being agitated occasionally. The catalyst material was then heated for 12 h at 100 °C before being calcined for 4 h at 700 °C in an electric furnace.[47]

2.2. Catalyst characterization study

Crystallographic tests were carried out using a Cu Ka radiation source and an X-ray diffractometer (Rigaku Miniflex II). The catalyst's functional group was identified using Fourier transform infrared spectra (FTIR; PerkinElmer). The Micromeritics ASAP2020 equipment was employed to measure the synthesized catalyst's surface exposed area and pore volume. High-resolution scanning electron microscopy was utilized to take pictures of the materials on a Hitachi S-4800 device (HR-SEM). High-resolution transmission electron microscopy (HR-TEM) pictures of the samples were captured using JEOL equipment (JEM 2010). In order to capture thermogravimetric data from the samples, we used a thermogravimetric analyser made by PerkinElmer with model number TGA 7. At room temperature, a PerkinElmer Fourier transform infrared (FTIR) spectrometer was utilized to record the as-synthesized samples by using the KBR pellet approach.

2.3. Catalytic activity in the selective oxidation of benzyl alcohol

Benzyl alcohol (BzOH – 20 mmol) was oxidized over 0.1 g of various 7% Ni and Fe catalysts (NFS-15) in a batch reactor (round bottom flask with Liebig condenser and temperature controller) utilizing *tert*-butyl hydroperoxide (TBHP – 25 mmol) as the oxidant and acetonitrile (10 ml) as the solvent. The aforementioned combination was thereafter heated at 100 °C for 7 hours. The products were identified using a gas

chromatograph with a flame ionization detector and a capillary column composed of 70 percent cyanopropyl polysphenylene siloxane, known as SGEBPX70, with the following specifications: 0.54 mm (length), 30 m (internal diameter), and 0.60 m (film thickness). The impacts of altering experimental parameters, such as concentration (7wt%Ni/SBA-15, 5wt%Ni-2wt%Fe/SBA-15, 4wt%Ni-3wt%Fe/SBA-15), catalyst loading (0.00–0.15 g), process temperature (50 to 110 °C), and TBHP/BzOH ratio (0.25–2.00), were assessed using the most active sample, Ni/Fe-SBA-15. Optimizing the process parameters maximized the BzOH conversion and benzaldehyde (BzH) selectivity. The possibility of recycling the sample was also checked.

3. Results and discussion

3.1. Characterization using spectroscopy and physicochemical

3.1.1. X-ray diffraction analysis (XRD). Fig. 1A illustrates the XRD profiles of the mono-and bi-metallic nickel-iron oxides promoted by SBA-15 catalysts and the *in situ* self-assembled core–shell precursor technique adopting oleic acid as the precursor. Fig. 1A displays a broad signal around 25° 2θ illustrates the presence of amorphous SiO_2. The broad diffraction peak located in the 2θ range of 15–40° is assigned to the SiO_2-based support. Similar to the previous investigation,[48] there is clear evidence of small particles of Ni and Fe on the support that is incredibly evenly spaced out. Additionally, the bimetallic phases of metallic Ni/Ni–Fe are challenging to differentiate when the catalyst samples were reduced for 1 hour at 700 °C.[49] The low angle XRD patterns of the SBA-15 and SZ/SBA-15 samples are shown in Fig. 1B. The patterns seen in the SBA-15 sample are those that were predicted for the sample. However, after loading each of the catalyst components, namely Ni, and Fe, a continuous decreasing trend in peak intensity is observed, revealing a steady decline in the mesoporous structure's orderliness as a result of successive impregnation and calcination.[50] Additionally, the location of the lines has slightly

Table 1 Surface areas and pore volumes of the catalysts

Catalyst	$S_{BET}{}^a$ $(m^2\ g^{-1})$	Pore volume[b] $(cm^3\ g^{-1})$	$D_p{}^c$ (nm)	$d_{100}{}^d$ (nm)
7Ni/SBA-15	698.12	0.720	7.14	0.80
5Ni–2Fe/SBA-15	652.80	0.692	7.05	0.84
4Ni–3Fe/SBA-15	642.38	0.681	7.00	1.08

^{a} Specific surface area by BET analysis. ^{b} Total pore volume estimated at $P/P_0 = 0.99$. ^{c} Average pore diameter calculated by Barrett–Joyner–Halenda (BJH) method. ^{d} From low angle XRD pattern (Fig. 1B).

shifted toward bigger angles [Table 1]. Previous studies hypothesized that such a change may be brought on by the deposition of oxides within the pores of SBA-15.[51] Owing to shifting peaks even when small amounts of Ni and Fe are loaded (Fig. 1A), it is likely that the shift in this state was caused by changes to the pore's structure.

3.1.2. BET surface area analysis. According to BET analysis, the adsorption–desorption isotherms for N_2 are shown in Fig. 2, each of the catalyst samples at varied relative pressures (P/P_0). According to IUPAC classification, the isotherms of the various Ni–Fe/SBA-15 catalysts that have been synthesized exhibit type IV Langmuir isotherms with H1-shaped hysteresis loops. The hysteresis loop of type H1 denotes network effects that existent in a complex mesoporous structure and are important, promoters that could result in remodelling or geometrical structural modifications to the active zones on the metal surface.[52] Despite loading Ni and Fe, there is considerable distortion in the hysteresis loop, a phenomenon that is typical of the behaviour anticipated for a substance with unified pores.

Table 1 also provides a summary of the catalyst's physical textural characteristics. Due to the mesoporous SBA-15 support's intrinsic properties, as well as every sample of the catalyst examined possessing a sizable specified surface area. In fact, compared to the Ni/SBA-15 monometallic catalyst, the
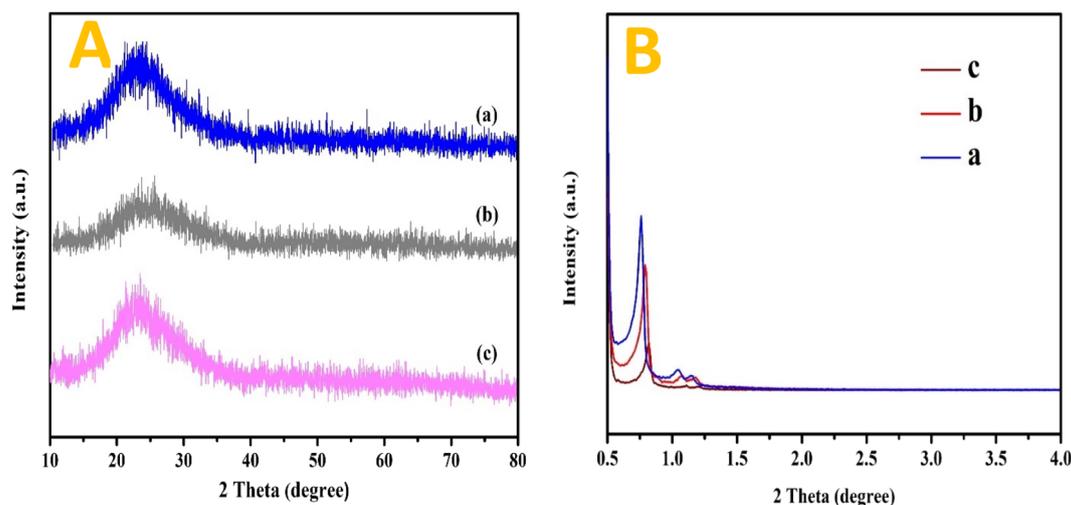

Fig. 1 (A) High angle XRD spectra of (a) 7wt%Ni/SBA-15, (b) 5wt%Ni-2wt%Fe/SBA-15, and (c) 4wt%Ni-3wt%Fe/SBA-15. (B) Low angle XRD spectra of (a) 7wt%Ni/SBA-15, (b) 5wt%Ni-2wt%Fe/SBA-15, and (c) 4wt%Ni-3wt%Fe/SBA-15.
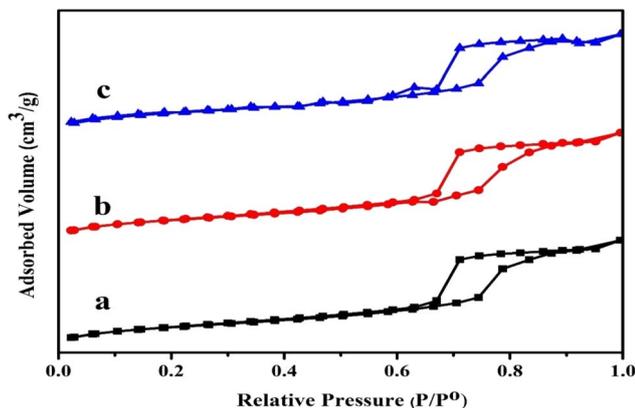
Fig. 2 BET isotherm of (a) 7wt%Ni/SBA-15, (b) 5wt%Ni-2wt%Fe/SBA-15, and (c) 4wt%Ni-3wt%Fe/SBA-15.

surface area would have been around 698.12 m^2 g$_{cat}^{-1}$, and the surface area decreased to approximately 642.38 m^2 g$_{cat}^{-1}$ when the Ni metal was substituted with merely 2 wt% Fe. However, the subsequent substitution of Ni metal up to 3 wt% Fe did not exhibit a material surface area that differed noticeably from the substitute of 2 weight percent Fe. The pore volume, meanwhile, gradually reduced from 0.72 with an upsurge in the Fe loading.[53] Furthermore, the pore capacity marginally decreased from 0.72 to 0.68 cm^3 g$_{cat}^{-1}$ with an increase in Fe loading. Reduction in the specific surface area from 698.12 m^2 g^{-1} of SBA-15 to 642.38 m^2 g^{-1} after metal loading could be attributed to the surface coverage by metal species, while no clear fluctuation in pore volume and average pore diameter indicated metal species might be mainly loaded on the exterior surface of SBA-15 by impregnation, without blocking the pore channels. As

a whole, the mass transfer resistance of something like the catalyst's pore network containing the hydrocarbon feed may be decreased by the existence of bigger pores. However, the pore diameter with Fe was slightly smaller, at about 7.00 nm, compared to the unsubstituted Ni/SBA-15 catalyst's 7.14 nm. These findings suggest that combining with Fe atoms causes the metals to migrate further deeper inside the host matrix of mesoporous silica, which results in a bit of constriction among the walls. However, the difference in pore size is only noticeably significant since the Fe atomic radius (126 pm) is not appreciably more important than that of Ni (124 pm).[54]

3.1.3. High-resolution transmission electron microscopy analysis (HR-TEM). The topologies of the reduced Ni–Fe bimetallic catalysts are exhibited in the TEM images in Fig. 3. It is easy to see the distinctive hexagonally organised SBA-15 mesoporous channels, which contain metallic elements inside or close to the mesoporous walls. Additionally, Particle sizes are typically less than 5 nm for all Ni/Ni–Fe compositions, with an average of 2–3 nm, as evidenced by the TEM images of each sample. These findings support the metallic size on a small scale that was suggested by the XRD results. The actual Ni/Fe weight ratios are 5.32 and 5.45 at two different locations, as seen from the data. This outcome exhibits the even dispersion of both Ni and Fe species across the catalytic support.[55,56]

3.1.4. High-resolution scanning electron microscopy analysis (HR-SEM). Utilizing a high-resolution scanning electron microscope, surface morphologies of Ni–Fe/SBA-15 were captured (HR-SEM). The HR-SEM images of Ni–Fe/SBA-15 generated using the approach are shown in Fig. 4a, b and c, respectively. The uniformly sized, spherical particles of Ni–1Fe/SBA-15 are agglomerated, as evident in the HR-SEM illustration. Furthermore, the average grain size is less than 100 nm, and all
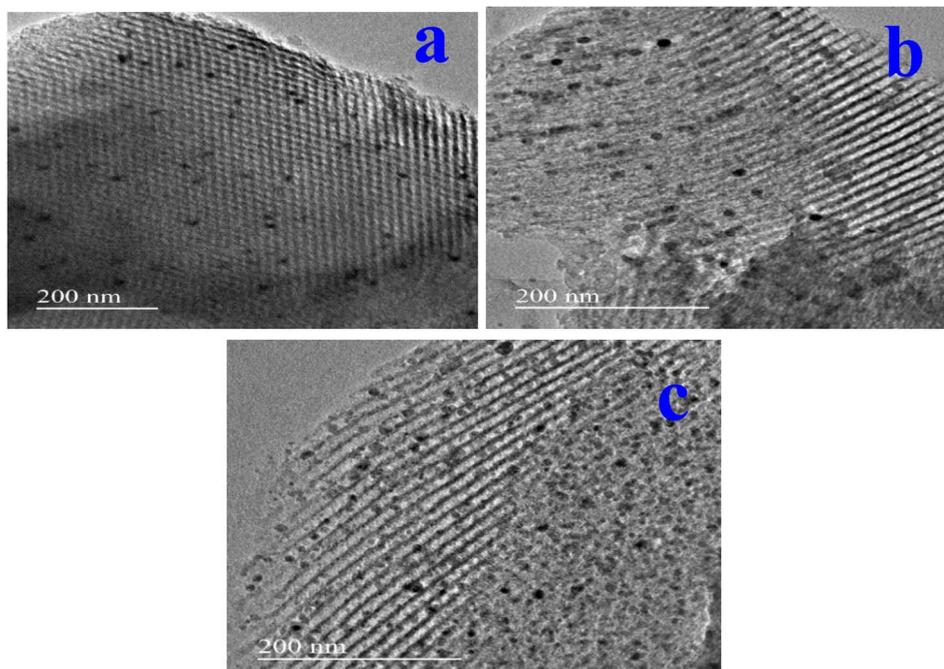

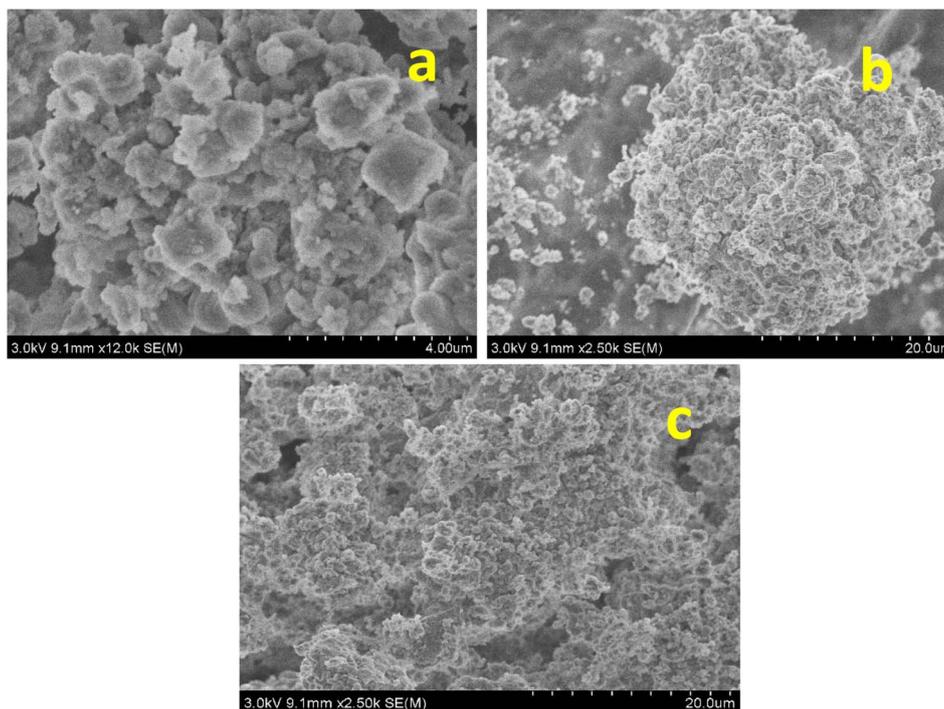**Fig. 3** TEM images of (a) 7wt%Ni/SBA-15, (b) 5wt%Ni-2wt%Fe/SBA-15, and (c) 4wt%Ni-3wt%Fe/SBA-15.

Fig. 4 SEM images of (a) 7wt%Ni/SBA-15, (b) 5wt%Ni-2wt%Fe/SBA-15, and (c) 4wt%Ni-3wt%Fe/SBA-15.

the particles are quite crystalline. Furthermore, it has been found that the metal nanoparticles were uniform in the 5wt% Ni-2wt%Fe/SBA-15 catalyst whereas agglomerated in the 7wt% Ni/SBA-15 catalyst with particle sizes of 22.34, 18.03, and 18.44 nm, respectively.

3.1.5. Thermal gravimetric analysis (TGA). Fig. 5 displays the results of a thermo gravimetric analysis of Ni–Fe bimetallic

SBA-15 synthesized using the impregnation processes. SBA-15 has strong thermal stability and doesn't lose much weight because its breakdown may be seen up to 700 °C. The minimal weight loss of the Ni–Fe/SBA-15 catalyst, which ranges from 1% to 4% and occurs between 100 and 150 C, is most likely the result of water that has been adsorbed onto the surface of the SBA-15. Interestingly, all Ni–Fe/SBA-15 catalysts exhibit a weight
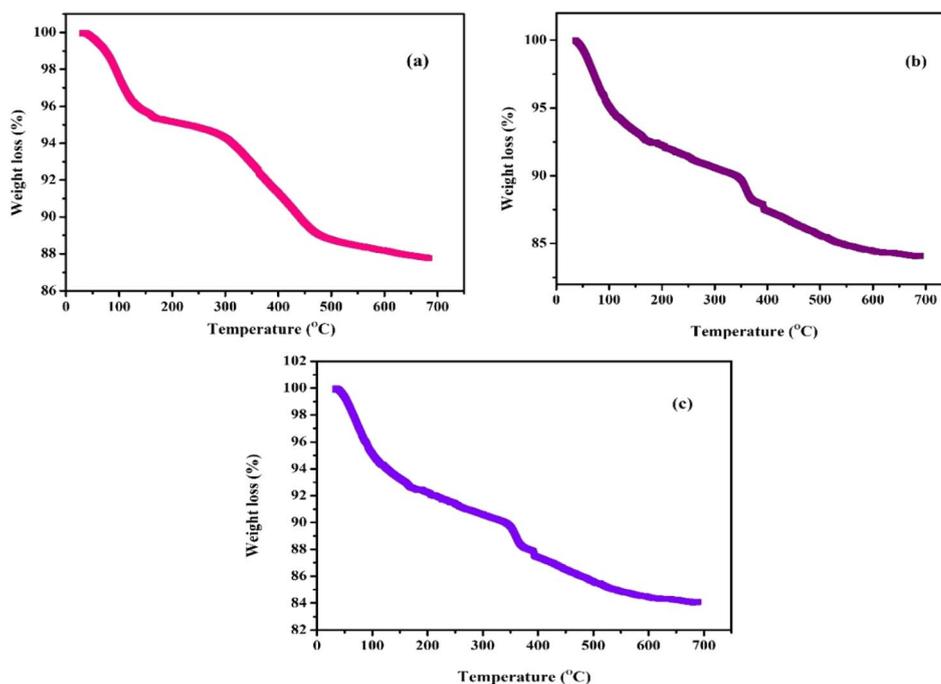

Fig. 5 TGA spectra of (a) 7wt%Ni/SBA-15, (b) 5wt%Ni-2wt%Fe/SBA-15, and (c) 4wt%Ni-3wt%Fe/SBA-15.

loss around 8% between 100 and 200 °C. This is because it has greater moisture content due to its increased occupancy. The second inflection point, which occurs in the temperature range of 360 to 510 °C, shows a weight loss of around 10% in all the Ni–Fe/SBA-15 catalyst implying a breakdown of surface Si–O bond which result in weight loss. The protection offered by the Ni–Fe/SBA-15 shell is attributed to this deterioration.

4. Selective catalytic oxidation study

4.1. Catalytic activity of Ni/Fe-SBA-15 catalysts on the oxidation of benzyl alcohol

4.1.1. The impact of metal loading. The catalytic activity of catalysts with various metal loading percentages, such as 7wt% Ni/SBA-15, 5wt% Ni-2wt% Fe/SBA-15, and 4wt% Ni-3wt% Fe/SBA-15, was contrasted in Fig. 6. The quantity of Ni–Fe/SBA-15 atoms introduced into the mesoporous catalyst determines how acidic the catalyst is and hence provides the assessment base for the impact of metal enrichment on SBA-15 catalysts in the BzOH transition. In the SBA-15 sample, just 30% of the benzyl alcohol is transformed, whereas the addition of Ni–Fe accelerates the conversion from 30% to a maximum of 90%. On the other hand, benzaldehyde's selectivity showed marginal improvement from 90 to 95% with the addition of bimetals. The addition of metal content shows a profound improvement in the conversion rate.[57] The metal content combination of 5wt% Ni-2wt% Fe/SBA-15 has provided the maximum conversion and selectivity of 90% and 95%, respectively. The results of the metal loading of 4wt% Ni-3wt% Fe/SBA-15 showed higher conversion and selectivity compared to 7wt% Ni/SBA-15 at 85% and 92%. However, the results of 4wt% Ni-3wt% Fe/SBA-15 were lower than 5wt% Ni-2wt% Fe/SBA-15, stressing the fact that the promoter role of Fe reaches its maximum at 2% loading. Again, due to a crowding effect between Ni and Fe, the catalytic efficiency at 4wt% Ni-3wt% Fe/SBA-15 is lower, which causes a drop in the conversion of benzyl alcohol. The optimum 5wt%Ni-
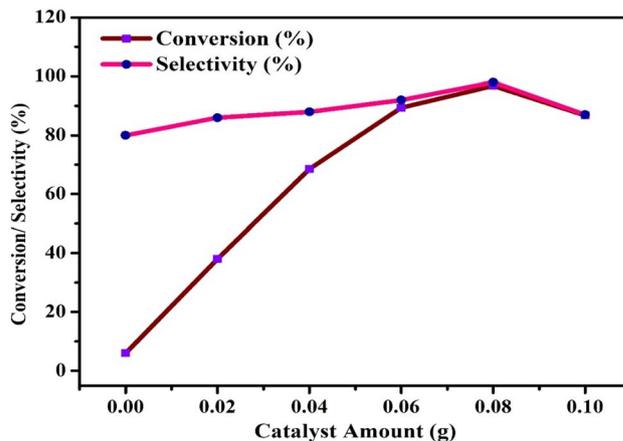

Fig. 7 Effect of catalyst amount on benzyl alcohol oxidation (conditions: BzOH – 20 mmol, NFS-15 catalyst, TBHP – 25 mmol, CH$_3$CN – 10 ml, 90 °C, time 7 h).

2wt%Fe/SBA-15 catalyst is therefore selected and is known as NFS-15 catalyst in the current study.[58]

4.1.2. Effect of catalyst weight. The 5wt% Ni-2wt% Fe/SBA-15 (NFS-15) catalyst was weighted in the range of 0.02 and 0.1 g to maximize the effect of catalyst concentration on BzOH conversion. The conversion trend shown in Fig. 7 demonstrates the importance of catalyst addition in enhancing the conversion of BzOH. The addition of catalyst from 0.02 to 0.08 g activates the process to improve the conversion rate from 38 to 92.5%. Due to a shortage of active sites, catalysts weighing 0.02 and 0.04 g have considerably low catalytic activity. Further adding of catalyst, the accessibility of the active zones is enhanced, aiding in the enhancement of reaction activity. As expected, increasing the catalyst's weight from 0.04 to 0.08 g improves conversion and selectivity. When the catalyst weight was increased from 0.08 to 0.10 g, the BzH selectivity decreased from 92.5 to 88.5%. Additionally, boosting the catalyst quantity to 0.10 g lowers
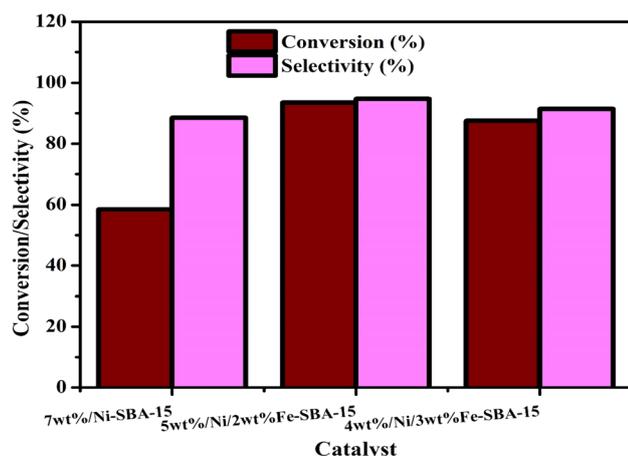

Fig. 6 Effect of metal loading on benzyl alcohol oxidation (conditions: BzOH – 20 mmol, catalysts – 0.08 g, TBHP – 25 mmol, CH$_3$CN – 10 ml, 90 °C, time 7 h).
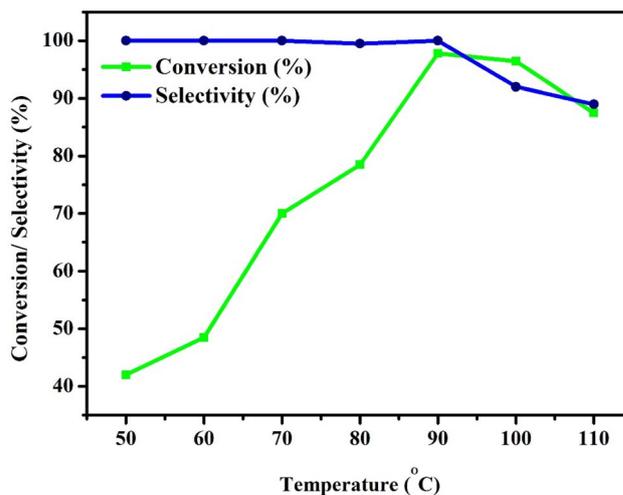

Fig. 8 Effect of reaction temperature on benzyl alcohol oxidation (conditions: BzOH 20 mmol, NFS-15 catalyst 0.08 g, TBHP 25 mmol, CH$_3$CN 10 ml, time 7 h).
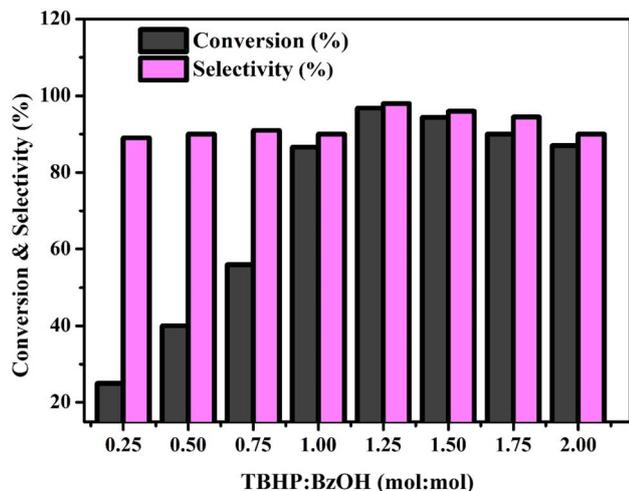
Fig. 9   Effect of TBHP/BzOH molar ratio on benzyl alcohol oxidation (conditions: BzOH – 20 mmol, NFS-5 catalyst – 0.08 g, CH$_3$CN – 10 ml, 90 °C, time 7 h).

conversion (88.5 percent), and the study shows that the optimum addition is 0.08 g. It was proposed that BzOH prevents benzoic acid from becoming benzaldehyde. The higher catalyst content can over-oxidise benzaldehyde to benzoic acid, which in turn can inhibit the conversion efficiency of the process. The lower selectivity at 0.1 g loading shows the possibility of the reaction by-products reducing the conversion rate of the catalyst.[59] Because much of the catalyst's catalytically active areas are hidden, all of the catalyst's adsorption zones are, therefore, inaccessible to reactant molecules. The selectivity of benzaldehyde reduces when 0.1 g of catalyst is employed for more than one reason. The catalyst concentration between 0.08 g and 0.1 g is remarkably different. We conclude that 0.08 g of catalyst is

ideal for getting the highest levels of selectivity and conversion based on the results.[60]

4.1.3.   Effect of the reaction temperature. The temperature of the reaction has a significant impact on BzOH conversion. We look into the effects of temperature at 50 to 110 °C. When the temperature is changed from 50 to 90 °C, the conversion increases from 30% to 92% (Fig. 8). The conversion and selectivity peaks to 99.5% and 100%, respectively at 90 °C. The conversion and selectivity dropped to 89.5% and 95.7% when the temperature was increased to 110 °C. The temperature significantly impacts the controlled kinetic process, which explains why the conversion of benzyl alcohol is poor at 50 and 60 °C. On the other hand, benzyl alcohol conversion and benzaldehyde selectivity decrease above 90 °C. While benzyl alcohol conversion is close to 88%, BzOH is lost due to the inhibitory effects. Furthermore, benzaldehyde transforms into benzoic acid at higher temperatures. According to the experimental results, 90 °C is the best temperature for maximizing BzOH conversion.[61]

4.1.4.   The effect of the substrate-to-oxidant ratio. The conversion of BzOH to benzaldehyde depends on the molar ratio of the oxidant to the substrate. From 0.25 to 2.00, the TBHP : BzOH ratio was examined. Fig. 9 shows how the TBHP/BzOH molar ratio affects the oxidation of benzyl alcohol. The proportion of conversion rises from 27% to 93.5% with a molar ratio increase from 0.25 to 1.25. According to the data, increasing the TBHP level significantly improves benzyl alcohol conversion.[62] To improve conversion, the TBHP : BzOH ratio must be greater than 1.25. The conversion rate of benzyl alcohol, even with a TBHP : BzOH ratio of 1.0, is lower than expected, and the same can be attributed to the fact that TBHP's ability to be oxidized declines after 88.5 percent conversion. At further increase beyond 1.25 and up to 2.00, the conversion of benzyl alcohol reduces to 87%, and selectivity drops to 88.6%.
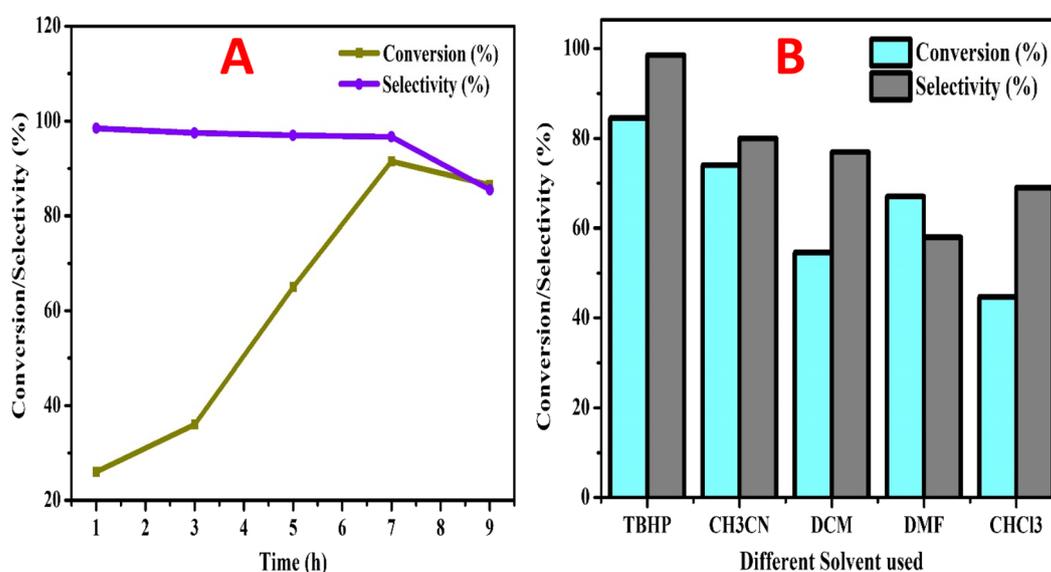

Fig. 10   (A) Effect of time (h) on benzyl alcohol oxidation (conditions: BzOH – 20 mmol, NFS-15 catalyst, TBHP – 25 mmol, NFS-5 catalyst – 0.1 g, CH$_3$CN – 10 ml, 90 °C). (B) Effect of solvent on benzyl alcohol oxidation (conditions: BzOH – 20 mmol, NFS-5 catalyst – 0.08 g, CH$_3$CN – 10 ml, 90 °C, time 7 h).

Table 2 Reusability studies of 6Ni–1Fe/SBA-15 sample

Catalyst	Run	1	2	3	4	5	6	7
NFS-15	Conversion	90	88.5	87.0	86.4	85.6	85.0	84.8
	Selectivity	97.5	96.4	98.8	98.4	97.6	94.6	93.6

This may be because TBHP, a chemical that readily transforms benzaldehyde into benzoic acid, decomposes under conditions of high oxygen concentration. Lower concentrations of TBHP result in restricted conversion, while higher concentrations of TBHP result in further oxidation. According to the experimental results, 1.25 is the perfect TBHP : BzOH ratio for the best BzOH transformation and BzH selectivity.[63]

4.1.5. The effect of time. Fig. 10A depicts the increasing reaction time from 1 h to 7 h with increasing benzaldehyde conversion from 28.5% to 92.8%. The hydrolysis of benzaldehyde resulted in a decrease in oxidizing selectivity. The optimal time for the reaction was discovered to be 7 hours.

4.1.6. The effect of the different solvents. The literature study revealed that the atmospheric liquid phase reaction, which affects both the reaction kinetics and product selectivity, plays numerous significant roles in the solvent impact. The protic solvent performs less well than the aprotic solvent in this situation due to the higher concentration of substrate near the catalyst's active sites. The solvent will become more polar and aprotic as the substrate density rises, which is advantageous to the catalytic process. *Tert*-butyl hydroperoxide (TBHP), chloroform, DMF, DCM, and acetonitrile are four distinct polarities of aprotic solvents used in our investigation. The TBHP oxidant produced the highest levels of benzaldehyde conversion and selectivity, as seen in Fig. 10B. TBHP has the highest dipole moment of all the oxidant examined. The conversion and selectivity achieved by TBHP were 85% and 99%, respectively.

4.1.7. Recyclability studies. The stability of catalysts and reusability is a crucial tools for industrial applications. The NFS-15 catalyst's stability was examined under ideal conditions (BzOH = 20 mmol, 5 wt% Ni and 2 wt% Fe/SBA-15 = 0.08 g, 25 mmol TBHP, 10 ml CH$_3$CN, 90 °C, and 4 hours), and the findings are reported in Table 2. Once the reaction is accomplished, the catalyst is filtered out from the reaction mixture, and the recovered catalyst is washed in ethanol before being dried at 110 °C in a hot air oven. The conversion of BzOH decreases from 90.0 percent to 84.8 percent after the fifth cycle, and the selectivity also decreases from 97.5% to 93.6%. As a result of catalyst loss during the recovery operations, selectivity and conversion somewhat decline after the fifth cycle. We infer from the experiment that 5 wt% Ni, 2 wt% Fe, and SBA-15 are better catalysts for converting BzOH. The aforementioned catalyst could be utilized on a large scale because it is easy to create, yields a superior amount of product, is cost-effective, and can be reused and recycled up to seven times.

4.1.8. Comparative catalytic activity. Studies on catalytic activity looked into a variety of parameters, such as temperature, pressure, catalyst, metals, conversion, and selectivity, that affected the oxidation of benzyl alcohol. An overview of the research on benzyl alcohol oxidation that we are comparing is provided in Table 3. In addition to being active, the catalyst identified in the current analysis continued to outperform other catalysts that have been reported.

5. Conclusion

Throughout this research, the efficacy of monometallic Ni supported on SBA-15 catalysts was compared to bimetallic Ni–Fe supported on SBA-15 catalysts for the selective oxidation of benzyl alcohol to benzaldehyde. A highly distributed Ni/FeSBA-15 catalyst based on SBA-15 was synthesized using the oleic acid aided incipient wetness impregnation approach. The NFS-15 catalyst achieved the highest rate of conversion and product selectivity. This could be as a result of the fact that NFS-15 exhibits a more synergistic interaction between Fe and Ni than the other catalysts produced in this study. The NFS-15 catalyst demonstrated 98% BzOH conversion and 99% BzH selectivity under optimised conditions (TBH P : BzOH ratio – 1.25; catalyst amount – 0.08 g; reaction temperature – 90 °C, reaction time 4 h). The NFS-15 catalyst's recycling effectiveness was evaluated up to 7 cycles, and it was discovered that the catalytic activity was sustained up to 7 cycles. This Ni and Fe loaded SBA-15 catalyst is affordable and efficient from an industrial perspective when compared to more costly metal catalysts. In terms of conversion, selectivity, and reaction temperature, the NFS-15 is not only better than other Ni-based catalysts mentioned in the literature, but it also outperforms them.

Table 3 Catalytic achievement of various catalysts in the oxidation of benzyl alcohol reaction

Catalyst entry	Catalyst dose (g)	Time (h)	Temperature (°C)	Conversion (%)	Selectivity (%) to aldehyde	References
TiMCM-41-20Ph-2(55)a	0.1	3	50	72	86	64
Anion resin H$_3$PW$_4$O$_{24}$	0.350	6	70	92.4	98.1	65
Ti(acac)-SBA-15	0.01	2	60	19.9	19.3	66
Ti(acac)-MCM-41 cal	0.01	2	60	8.1	7.5	67
10%Me-TiMCM-41NP	0.03	0.5	60	8.4	13.4	68
TiMCM-41 LP	0.03	2	70	5.7	10.3	69
Cu(II)-cyclamSBA-16	0.05	4	80	47.3	3.6	70
10 MeTiM-1	0.05	7	80	45.8	74.76	71
NFS-15	0.08	7	90	93.5	97.5	This work

Conflicts of interest

Acknowledgements

Notes and references

1 Z. Luo, A. S. Poyraz, C.-H. Kuo, R. Miao, Y. Meng, S.-Y. Chen, T. Jiang, C. Wenos and S. L. Suib, Crystalline Mixed Phase (Anatase/Rutile) Mesoporous Titanium Dioxides for Visible Light Photocatalytic Activity, *Chem. Mater.*, 2015, **27**, 6–17.

2 M. Fukui, W. Koshidaa, A. Tanakaa, K. Hashimotoa and H. Kominamia, Photocatalytic hydrogenation of nitrobenzenes to anilines over noble metal-free TiO2 utilizing methylamine as ahydrogen donor, *Appl. Catal., B*, 2020, **268**, 118446.

3 Z. Hu, H. Quan, Z. Chen, Y. Shao and D. Li, New insight into efficient visible-light-driven photocatalytic organic transformation over CdS/TiO2 photocatalysts, *Photochem. Photobiol. Sci.*, 2018, **17**, 51–59.

4 X. Li, J. Wang, Y. Men and Z. Bian, TiO2 mesocrystal with exposed (001) facets and CdS quantum dots as an active visible photocatalyst for selective oxidation reactions, *Appl. Catal., B*, 2016, **187**, 115–121.

5 N. Qin, Y. Liu, W. Wu, L. Shen, X. Chen, Z. Li and L. Wu, One Dimensional CdS/TiO2 Nanofiber Composites as Efficient Visible Light-Driven Photocatalysts for Selective Organic Transformation: Synthesis, Characterization, and Performance, *Langmuir*, 2015, **31**, 1203–1209.

6 M. Zhang, Q. Wang, C. Chen, L. Zang, W. Ma and J. Zhao, Oxygen Atom Transfer in the Photocatalytic Oxidation of Alcohols by TiO2: Oxygen Isotope Studies, *Angew. Chem., Int. Ed.*, 2009, **48**, 6081–6084.

7 K. Yaemsunthorn, M. Kobielusz and W. Macyk, TiO2 with Tunable Anatase-to-Rutile Nanoparticles Ratios: How Does the Photoactivity Depend on the Phase Composition and the Nature of Photocatalytic Reaction?, *ACS Appl. Nano Mater.*, 2021, **4**, 633–643.

8 J. Zhu, S. Zhu, X. Kong, Y. Liang, Z. Li, S. Wu, S. Luo, C. Chang and Z. Cui, Rutile-Coated B-Phase TiO2 Heterojunction Nanobelts for Photocatalytic H2 Evolution, *ACS Appl. Nano Mater.*, 2020, **3**, 10349–10359.

9 A. J. Gardecka, C. Bishop, D. Lee, S. Corby, I. P. Parkin, A. Kafizas and S. Krumdieck, High efficiency water splitting photoanodes composed of nano-structured anatase-rutile TiO2 heterojunctions by pulsed-pressure MOCVD, *Appl. Catal., B*, 2018, **224**, 904–911.

10 J. Schneider, M. Matsuoka, M. Takeuchi, J. Zhang, Y. Horiuchi, M. Anpo and D. W. Bahnemann, Understanding TiO2 Photocatalysis: Mechanisms and Materials, *Chem. Rev.*, 2014, **114**, 9919–9986.

11 M. Pelaez, N. T. Nolan, S. C. Pillai, M. K. Seery, P. Falaras, A. G. Kontos, P. S. M. Dunlope, J. W. J. Hamiltone, J. A. Byrnee, K. O'Sheaf, M. H. Entezarig and D. D. Dionysioua, A Review on The Visible Light Active Titanium Dioxide Photocatalysts for Environmental Applications, *Appl. Catal., B*, 2012, **125**, 331–349.

12 J. Harris, R. Silk, M. Smith, Y. Dong, W.-T. Chen and G. I. N. Waterhouse, Hierarchical TiO2 Nanoflower Photocatalysts with Remarkable Activity for Aqueous Methylene Blue PhotoOxidation, *ACS Omega*, 2020, **5**, 18919–18934.

13 M. Toyoda, Y. Nanbu, Y. Nakazawa, M. Hirano and M. Inagaki, Effect of crystallinity of anatase on photoactivity for methylene blue decomposition in water, *Appl. Catal., B*, 2004, **49**, 227–232.

14 V. Etacheri, M. K. Seery, S. J. Hinder and S. C. Pillai, Highly Visible Light Active TiO2-xNx Heterojunction Photocatalysts, *Chem. Mater.*, 2010, **22**, 3843–3853.

15 V. Kumaravel, S. Mathew, J. Bartlett and S. C. Pillai, Photocatalytic hydrogen production using metal doped TiO2: A review of recent advances, *Appl. Catal., B*, 2019, **244**, 1021–1064.

16 N. Serpone, Is the Band Gap of Pristine TiO2 Narrowed by Anion and Cation-Doping of Titanium Dioxide in Second-Generation Photocatalysts?, *J. Phys. Chem. B*, 2006, **110**, 24287–24293.

17 R. Asahi, T. Morikawa, T. Ohwaki, K. Aoki and Y. Taga, VisibleLight Induced Photocatalysis in Nitrogen doped Titanium Dioxides, *Science*, 2001, **293**, 269–271.

18 X. Pan, M.-Q. Yang, X. Fu, N. Zhang and Y.-J. Xu, Defective TiO2 with oxygen vacancies: synthesis, properties and photocatalytic applications, *Nanoscale*, 2013, **5**, 3601–3614.

19 X. Zhang, Y. Wang, B. Liu, Y. Sang and H. Liu, Heterostructures construction on TiO2 nanobelts: A powerful tool for building high-performance photo catalysts, *Appl. Catal., B*, 2017, **202**, 620–641.

20 R. I. Bickley, T. G. Carreno, J. S. Lee, L. Palmisano and R. J. D. Tilley, A Structural Investigation of Titanium Dioxide Photocatalysts, *J. Solid State Chem.*, 1991, **92**, 178–190.

21 D. O. Scanlon, C. W. Dunnill, J. Buckeridge, S. A. Shevlin, A. J. Logsdail, S. M. Woodley, C. R. A. Catlow, M. J. Powell, R. G. Palgrave, I. P. Parkin, G. W. Watson, T. W. Keal, P. Sherwood, A. Walsh and A. A. Sokol, Band Alignment of Rutile and Anatase TiO2, *Nat. Mater.*, 2013, **12**, 798–801.

22 X. Zhou, E. Wierzbicka, N. Liu and P. Schmuki, Black and white anatase, rutile and mixed forms: band-edges and photocatalytic activity, *Chem. Commun.*, 2019, **55**, 533–536.

23 D. C. Hurum, A. G. Agrios, K. A. Gray, T. Rajh and M. C. Thurnauer, Explaining the Enhanced Photocatalytic Activity of Degussa P25 Mixed-Phase TiO2 Using EPR, *J. Phys. Chem. B*, 2003, **107**, 4545–4549.

24 M. Nasrollahzadeh, M. Sajjadi, M. Shokouhimehr and R. S. Varma, Recent developments in palladium (nano) catalysts supported on polymers for selective and sustainable oxidation processes, *Coord. Chem. Rev.*, 2019, **397**, 54–75.

25 S. Sato, R. Nakamura and S. Abe, Visible-light sensitization of TiO2 photocatalysts by wet-method N doping, *Appl. Catal., A*, 2005, **284**, 131–137.

26 Z. Liu, X. Zhang, S. Nishimoto, M. Jin, D. A. Tryk, T. Murakami and A. Fujishima, Anatase TiO2 Nanoparticles on Rutile TiO$_2$Nanorods: A Heterogeneous Nanostructure via Layer-by-Layer Assembly, *Langmuir*, 2007, **23**, 10916–10919.

27 Z. Xing, J. Zhang, J. Cui, J. Yin, T. Zhao, J. Kuang, Z. Xiu, N. Wan and W. Zhou, Recent advances in floating TiO2-basedphotocatalysts for environmental application, *Appl. Catal., B*, 2018, **225**, 452–467.

28 B. R. Venugopal, E. P. Samuel, C. Shivakumara and M. Rajamathi, Macroporous metal oxide foams through self-sustained combustion reactions, *J. Porous Mater.*, 2009, **16**, 205–208.

29 B. R. Venugopal, S. Naik, M. Antony, G. Ramalingam, M. Rajamathi and S. Raghavan, Amorphous, Monoclinic, and Tetragonal Porous Zirconia Through a Controlled Self-Sustained Combustion Route, *J. Am. Ceram. Soc.*, 2011, **94**, 1747–1755.

30 K. Nagaveni, M. S. Hegde, N. Ravishankar, G. N. Subbanna and G. Madras, Synthesis and Structure of Nanocrystalline TiO2 with Lower Band Gap Showing High Photocatalytic Activity, *Langmuir*, 2004, **20**, 2900–2907.

31 S. Sakthivel and H. Kisch, Daylight Photocatalysis by CarbonModified Titanium Dioxide, *Angew. Chem., Int. Ed.*, 2003, **42**, 4908–4911.

32 S. U. M. Khan, M. Al-Shahry and W. B. Ingler Jr, Efficient Photochemical Water Splitting by a Chemically Modified n-TiO2, *Science*, 2002, **297**, 2243–2245.

33 K. Nagaveni, G. Sivalingam, M. S. Hegde and M. Giridhar, Solar photocatalytic degradation of dyes: high activity of combustion synthesized nano TiO2, *Appl. Catal., B*, 2004, **48**, 83–93.

34 D. A. H. Hanaor and C. C. Sorrell, Review of the anatase to rutile phase transformation, *J. Mater. Sci.*, 2011, **46**, 855–874.

35 S. Yurdakal, G. Palmisano, V. Loddo, V. Augugliaro and L. Palmisano, Nanostructured Rutile TiO2 for Selective Photocatalytic Oxidation of Aromatic Alcohols to Aldehydes in Water, *J. Am. Chem. Soc.*, 2008, **130**, 1568–1569.

36 G.-J. T. Brink, I. W. C. E. Arends and R. A. Sheldon, Green, Catalytic Oxidation of Alcohols in Water, *Science*, 2000, **287**, 1636–1639.

37 M. R. Hoffmann, S. T. Martin, W. Choi and D. W. Bahnemann, Environmental Applications of Semiconductor Photocatalysis, *Chem. Rev.*, 1995, **95**, 69–96.

38 T. Mallat and A. Baiker, Oxidation of Alcohols with Molecular Oxygen on Solid Catalysts, *Chem. Rev.*, 2004, **104**, 3037–3058.

39 Y. Shiraishi, N. Saito and T. Hirai, Titanosilicate Molecular Sieve for Size-Screening Photocatalytic Conversion, *J. Am. Chem. Soc.*, 2005, **127**, 8304–8306.

40 R. Li, Y. Zhang, B. Xing, M. Huang, T. Wang, X. Hong, B. Zhou, B. Li, D. Jia and S. Qi, Modulating the electronic structure of Co-Ni bimetal oxides on mesoporous silica for promoting selective oxidation of alcohol, *Microporous Mesoporous Mater.*, 2023, **350**, 112407.

41 X. Zhang, F. Bi, Z. Zhu, Y. Yang, S. Zhao, J. Chen, X. Lv, Y. Wang, J. Xu and N. Liu, The promoting effect of H$_2$O on rod-like MnCeO$_x$ derived from MOFs for toluene oxidation: A combined experimental and theoretical investigation, *Appl. Catal., B*, 2021, **297**, 120393.

42 R. Tadmor, R. E. Rosensweig, J. Frey and J. Klein, Resolving the Puzzle of Ferrofluid Dispersants, *Langmuir*, 2000, **16**, 9117–9120.

43 T. Gong, D. Yang, J. Hu, W. Yang, C. Wang and J. Q. Lu, Preparation of monodispersed hybrid nanospheres with high magnetite content from uniform Fe3O4 clusters, *Colloids Surf., A*, 2009, **339**, 232–239.

44 Y. Lu, X. Lu, T. Brian, T. H. Mayers and Y. Xia, Synthesis and characterization of magnetic Co nanoparticles: A comparison study of three different capping surfactants, *J. Solid State Chem.*, 2008, **181**, 1530–1538.

45 W.-T. Chen, A. G. Dosado, A. Chan, D. S. Waterhouse and G. I. N. Waterhouse, Highly Reactive Anatase Nanorod Photocatalysts Synthesized by Calcination of Hydrogen Titanate Nanotubes: Effect of Calcination Conditions on Photocatalytic Performance for Aqueous Dye Degradation and H2 Production in Alcohol-Water Mixtures, *Appl. Catal., A*, 2018, **565**, 98–118.

46 H. Xu, G. Li, G. Zhu, K. Zhu and S. Jin, Enhanced Photocatalytic Degradation of Rutile/Anatase TiO2 Heterojunction Nano flowers, *Catal. Commun.*, 2015, **62**, 52–56.

47 G. Lui, J.-Y. Liao, A. Duan, Z. Zhang, M. Fowler and A. Yu, Graphene-Wrapped Hierarchical TiO2 Nano flower Composites with Enhanced Photocatalytic Performance, *J. Mater. Chem. A*, 2013, **1**, 12255–12262.

48 H. Choi, A. C. Sofranko and D. D. Dionysiou, Nanocrystalline TiO2 Photocatalytic Membranes with a Hierarchical Mesoporous Multilayer Structure: Synthesis, Characterization, and Multifunction, *Adv. Funct. Mater.*, 2006, **16**, 1067–1074.

49 H. Maleki and V. Bertola, TiO$_2$ Nanofilms on Polymeric Substrates for the Photocatalytic Degradation of Methylene Blue, *ACS Appl. Nano Mater.*, 2019, **2**, 7237–7244.

50 M.-C. Wu, K.-C. Hsiao, Y.-H. Chang and K. Kordás, Core−Shell Heterostructures of Rutile and Anatase TiO$_2$ Nanofibers for Photocatalytic Solar Energy Conversion, *ACS Appl. Nano Mater.*, 2019, **2**, 1970–1979.

51 J. Huo, C. Yuan and Y. Wang, Nanocomposites of ThreeDimensionally Ordered Porous TiO$_2$ Decorated with Pt and Reduced Graphene Oxide for the Visible-Light Photocatalytic Degradation of Waterborne Pollutants, *ACS Appl. Nano Mater.*, 2019, **2**, 2713–2724.

52 Z. He, Q. Cai, H. Fang, G. Situ, J. Qiu, S. Song and J. Chen, Photocatalytic Activity of TiO$_2$ Containing Anatase Nanoparticles and Rutile Nanoflower Structure Consisting of Nanorods, *J. Environ. Sci.*, 2013, **25**, 2460–2468.

53 L. Yu, Y. Lin and D. Li, Visible-light-induced aerobic oxidation of alcohols in a green catalytic system of

carbonate-like species doped TiO2, *Appl. Catal., B*, 2017, **216**, 88–94.

54 D. I. Enache, D. Barker, J. K. Edwards, S. H. Taylor, D. W. Knight, A. F. Carley and G. J. Hutchings, Solvent-free oxidation of benzyl alcohol using titania-supported gold–palladium catalysts: effect of Au–Pd ratio on catalytic performance, *Catal. Today*, 2007, **122**(3–4), 407–411.

55 G. Gao, R. Rong, Z. Zhang, B. Pan, X. Sun, Q. Zhang, G. Zheng, K. Xu and L. GaoIn, Selective oxidation of benzyl alcohol to benzaldehyde over $CoFe_2O_4$ nanocatalyst, *Catal. Commun.*, 2023, **183**, 106757.

56 J. Tsuji, Synthetic Applications of the Palladium-Catalyzed Oxidation of Olefins to Ketones, *Synthesis*, 1984, **1984**, 369–384.

57 M. A. Fouad, H. Abdel-Hamid and M. S. Ayoup, Two decades of recent advances of Ugi reactions: synthetic and pharmaceutical applications, *RSC Adv.*, 2020, **10**, 42644–42681.

58 S. Semwal and J. Choudhury, Switch in Catalyst State: Single Bifunctional Bi-state Catalyst for Two Different Reactions, *Angew. Chem., Int. Ed.*, 2017, **56**, 5556–5560.

59 L. Liu, S. Zhang, X. Fu and C.-H. Yan, Metal-free aerobic oxidative coupling of amines to imines, *Chem. Commun.*, 2011, **47**, 10148–10150.

60 F. Bottaro, A. Takallou, A. Chehaiber and R. Madsen, CobaltCatalyzed Dehydrogenative Coupling of Amines into Imines, *Eur. J. Org Chem.*, 2019, **2019**, 7164–7168.

61 T. Xiao, S. Xiong, Y. Xie, X. Dong and L. Zhou, Coppercatalyzed synthesis of benzazoles via aerobic oxidative condensation of o-amino/mercaptan/hydroxyanilines with benzylamines, *RSC Adv.*, 2013, **3**, 15592–15595.

62 K. Singh, A. Kaur, V. S. Mithu and S. Sharma, Metal-Free Organocatalytic Oxidative Ugi Reaction Promoted by Hypervalent Iodine, *J. Org. Chem.*, 2017, **82**, 5285–5293.

63 K. Kaizuka, H. Miyamura and S. Kobayashi, Remarkable effect of bimetallic nanocluster catalysts for aerobic oxidation of alcohols: combining metals changes the activities and the reaction pathways to aldehydes/carboxylic acids or esters, *J. Am. Chem. Soc.*, 2010, **132**, 15096–15098.

64 M. Shibasaki and Y. Yamamoto, *Multimetallic Catalysts in Organic Synthesis*, Wiley, Weinheim, Germany, 2006.

65 I. Bratko and M. Gomez, Polymetallic complexes linked to a single-frame ligand: cooperative effects in catalysis, *Dalton Trans.*, 2013, **42**, 10664–10681.

66 M. Shibasaki, M. Kanai, S. Matsunaga and N. Kumagai, Recent progress in asymmetric bifunctional catalysis using multimetallic systems, *Acc. Chem. Res.*, 2009, **42**, 1117–1127.

67 M. Sankar, N. Dimitratos, P. J. Miedziak, P. P. Wells, C. J. Kiely and G. J. Hutchings, Designing bimetallic catalysts for a green and sustainable future, *Chem. Soc. Rev.*, 2012, **41**, 8099–8139.

68 C. Kaub, S. Lebedkin, A. Li, S. V. Kruppa, P. H. Strebert, M. M. Kappes, C. Riehn and P. W. Roesky, Bimetallic d10-metal complexes of a bipyridine substituted N-heterocyclic carbene, *Chem.–Eur. J.*, 2018, **24**, 6094–6104.

69 T. Dang-Bao, D. Pla, I. Favier and M. Gomez, Bimetallic nanoparticles in alternative solvents for catalytic purposes, *Catalysts*, 2017, **7**, 207.

70 C. Parmeggiani and F. Cardona, Transition metal based catalysts in the aerobic oxidation of alcohols, *Green Chem.*, 2012, **14**, 547–564.

71 T. Punniyamurthy, S. Velusamy and J. Iqbal, Recent advances in transition metal catalyzed oxidation of organic substrates with molecular oxygen, *Chem. Rev.*, 2005, **105**, 2329–2364.